Using a Multi-Physics Ensemble for Exploring Diversity in Cloud-Shortwave Feedback in GCMs

Masahiro Watanabe[1], Hideo Shiogama[2], Tokuta Yokohata[2], Youichi Kamae[1], Masakazu Yoshimori[1], Tomoo Ogura[2], James D Annan[3], Julia C Hargreaves[3], Seita Emori[1,2], and Masahide Kimoto[1]

1: Atmosphere and Ocean Research Institute, University of Tokyo
2: National Institute for Environmental Studies
3: Research Institute for Global Change, JAMSTEC

Journal of Climate

Submitted on September 30, 2011

Corresponding author:
M. Watanabe, Atmosphere and Ocean Research Institute, University of Tokyo,
5-1-5 Kashiwanoha, Kashiwa, Chiba 277-8568, Japan.
E-mail: hiro@aori.u-tokyo.ac.jp

ABSTRACT

This study proposes a systematic approach to investigate cloud-radiative feedbacks to increase of CO_2 concentrations in global climate models (GCMs). Based on two versions of the Model for Interdisciplinary Research on Climate (MIROC), which have opposite signs for cloud-shortwave feedback (ΔSW_{cld}) and hence different equilibrium climate sensitivities (ECS), we construct hybrid models by replacing one or more parameterization schemes for cumulus convection, cloud, and the turbulence between them. An ensemble of climate change simulations using a suite of eight models, called a multi-physics ensemble (MPE), is generated. The MPE provides a range of ECS as wide as the CMIP3 multi-model ensemble and reveals a different magnitude and sign of ΔSW_{cld} over the tropics, which is crucial for determining ECS.

It is found that no single process controls ΔSW_{cld}, but that the coupling of two processes does. Namely, changing the cloud and turbulence schemes greatly alters the mean and the response of low clouds, whereas replacing the convection and cloud schemes affects low and middle clouds over the convective region. For each of the circulation regimes, ΔSW_{cld} and cloud changes in the MPE have a nonlinear, but systematic, relationship with the mean cloud amount, which may be constrained from satellite estimates. The analysis suggests a positive feedback over the subsidence regime and a near-neutral or weak negative ΔSW_{cld} over the convective regime.

1. Introduction

The global climate model (GCM) is a unique tool for physically-based simulations of the Earth's climate. GCMs have been improved during the past three phases of the Coupled Model Intercomparison Project (CMIP) (Reichler and Kim 2008) and extensively used in the Intergovernmental Panel on Climate Change (IPCC) Assessment Reports (Solomon et al. 2007). While many aspects of the climate simulated in GCMs, such as temperature and wind fields, are much more realistic than in the past, the representation of clouds remains one of their largest limitations. Indeed, the current IPCC-class models show a substantial divergence in terms of sign and magnitude of the cloud-radiative feedback in response to an increase in atmospheric CO_2 concentration (e.g., Bony and Dufresne 2005; Soden and Held 2006; Webb et al. 2006).

Since the dynamical core is more or less similar in the current generation GCMs, the diversity of the cloud feedback is recognized to arise mostly from different parameterization schemes for unresolved physical processes in the atmosphere. While the CMIP phase 3 (CMIP3) provides experimental data from 23 GCMs and enables various analyses, the multi-model ensemble (MME) alone is insufficient to understand the source of cloud feedback diversity because the models are structurally different from one another.

There are three alternatives for dealing with the diversity in the cloud feedback and equilibrium climate sensitivity (ECS) in GCMs, as schematically presented in Fig. 1. Given that the CMIP models show cloud feedback with increasing CO_2 level, varying both in magnitude and sign (grey "X"), each of these approaches first pick one or two particular models up (indicated by black marks in Fig. 1). When we perturb model parameters without changing the model code and perform CO_2 doubling (or equivalent) runs with each set of parameters, the model ensemble helps quantify the range of uncertainty in the feedback processes (e.g., Murphy et al. 2004; Stainforth et al. 2005). This type of ensemble, called a perturbed physics ensemble (PPE), has been generated by several modeling groups (Collins et al. 2010; Yokohata et al. 2010; Sanderson et al. 2010; Klocke et al. 2011), all of whom show that PPE is useful in quantifying climate change uncertainties due to model parameters. However, PPE is not necessarily suitable for exploring the feedback mechanism in the base model, on which the ensemble property crucially depends (Yokohata et al. 2010).

The second approach is to simplify the model's configuration from a realistic GCM to an idealized aqua planet, and to a single column, sharing the parameterization schemes. The use of such a hierarchy of models is relevant for understanding mechanisms of cloud feedback in a chosen GCM, as long as the simplified models reproduce the cloud and cloud-radiative properties in a full model (Zhang and Bretherton 2008; Medeiros et al. 2008). Brient and Bony (2011) showed that a single-column model (SCM) based on the IPSL CM5A GCM can reproduce the vertical profile of cloud fraction over the subsidence regime in the GCM. They then clarified the mechanism of the decrease of low clouds in the global warming simulation found there in. While the dominant process controlling cloud feedback in their GCM may not be operating in others (Wyant et al. 2009), the hierarchical modeling provides a process-based understanding of the cloud feedback.

The third approach, adopted in the present work, maintains the same level of complexity in the model configuration, but attempts to trace the source of different behavior between *two* GCMs. This is accomplished by replacing one or more parameterization schemes in the two models, and then evaluating the cloud feedback from each of the hybrid models. This ensemble, called a multi-physics ensemble (MPE) throughout this paper, directly solves the structural difference of the models, and is therefore conceptually different from PPEs. The MPE would be particularly helpful when we have models coded in a similar manner, e.g., different versions of a GCM, but exhibiting very different cloud feedback. While a few studies have applied MPE to numerical weather prediction (Houtekamer et al. 1996; Stensrud et al. 2000), there is little study that investigated diversity in the climate feedback using MPE due to the cost of constructing but not running the hybrid models. A recent work by Gettelman et al. (2011) is an exception, in which they swapped cloud macro/microphysics, radiation, aerosol, turbulence, and shallow convection schemes between two versions of the NCAR Community Atmospheric Model (CAM) in order to find the reason for their different climate sensitivities. They found that the newer version of CAM5 has a higher ECS associated with the positive cloud-shortwave feedback (ΔSW_{cld}) over the trade cumulus region and the mid-latitude storm tracks, which is mainly due to the updated shallow convection scheme.

With the aim of contributing to the IPCC Fifth Assessment Report (AR5), we have continuously developed our GCM, called the Model for Interdisciplinary Research on Climate (MIROC). In a new version of MIROC5, many climate aspects have been improved by not only increasing the resolution but also updating the parameterization schemes (Watanabe et al. 2010). Of particular interest is that MIROC5 has a lower ECS (2.6 K) than the previous version, MIROC3.2 (3.6 K), and this is attributed to the difference in the cloud-shortwave feedback (Watanabe et al. 2011a, 2011b). In the present study, a MPE is constructed on the basis of these two models in order to understand crucial processes controlling the cloud-shortwave feedback, and hence ECS. We have also made PPEs using both MIROC3.2 and MIROC5 (Yokohata et al. 2010;

Shiogama et al. 2011), enabling us to anlayze them together in some parts of the paper, which will demonstrate the efficacy of the MPE.

The present paper is organized as follows. In section 2, ensembles based on the two versions of MIROC and the experimental designs are described. In section 3, we evaluate the range of ECS among PPEs and the MPE, and present that the cloud-shortwave feedback over the tropics is a major factor for different ECSs between the PPEs. The mean cloud fields and their response to surface warming are then analyzed in section 4. Composites sorted by the circulation regime indicate that a different set of the coupled physical processes has a dominant role in modulating cloud response at the convective and subsidence regimes. In section 5, a nonlinear relationship is identified between the cloud-shortwave feedback and the mean cloud amount in each regime, which is used to discuss the relative credibility of the cloud feedback mechanisms in the two versions of MIROC. Section 6 gives the concluding discussion.

2. Model ensembles

a. MIROC3 PPE

MIROC3.2, which was used for the CMIP3, has been jointly developed at the Centre for Climate System Research (CCSR)[1], the University of Tokyo, the National Institute for Environmental Studies (NIES), and the Japan Agency for Marine-Earth Science and Technology (JAMSTEC) (K-1 model developers 2004). When generating the PPE, the ocean component model has been replaced by a 50 m deep slab-ocean, and the horizontal resolution of the atmospheric component has been reduced from T42 to T21 to save computational effort. To ensure a realistic mean climatology, the so-called

[1] Renamed the Atmosphere and Ocean Research Institute as of April, 2011.

q-flux was applied to sea surface temperature (SST) and sea-ice distributions.

Among various techniques to perturb the system, the MIROC3.2 PPE (referred to as MIROC3 PPE-S in this study; “S” stands for the slab-ocean GCM) is generated following the methods of Annan et al. (2005) and Hargreaves et al. (2007) in the Japan Uncertainty Modelling Project (JUMP). Specifically, the model mean states were constrained by assimilating observations when determining optimal sets of perturbations for 13 parameters in the atmospheric component. Further details are described in Yokohata et al. (2010). We use 32 members, each of which consists of a 70 y control and a 2×CO_2 run.

b. MIROC5 PPEs

A PPE using MIROC5 was recently generated to evaluate the parametric uncertainty of the ECS obtained from the official version of MIROC5. This PPE can also be used for comparison with the MIROC3 PPE-S and PPEs from other GCMs in future work. As in the MIROC3 PPE-S, the horizontal resolution of the atmosphere model was reduced from the official configuration (from T85 to T42) after we confirmed that the essential property of the feedback and ECS is unchanged by this reduction. Unlike the previous PPE, however, we attempt to use the full coupled model to avoid any artificial influence of the q-flux on the ECS (Jackson et al. 2011). A thorough description of the method for generating perturbations is given by Shiogama et al. (2011), and is briefly explained below.

The procedure is divided into two parts. First, an ensemble of the atmosphere model (MIROC5 PPE-A; “A” stands for the atmosphere model) was generated by varying a single parameter to its maximum and minimum values, as determined by experts’ judgment. This was repeated for 20 pre-chosen parameters and one logical switch to yield a 42 member ensemble (including the standard setting), each consisting of a 6 y long integration of the control, 4×CO_2, and SST runs. In the former two, the SST and sea-ice concentration are prescribed by the control climatology of the full MIROC5, whereas the SST run is driven using the monthly climatology from an abrupt 4×CO_2 coupled model experiment (years 11-20). Time-mean differences in the top-of-atmosphere (TOA) radiative budgets for the last 5 years between the control and 4×CO_2 runs define the radiative forcing, and similarly the differences between the control and SST runs scaled by the global-mean surface air temperature (SAT) difference give the feedback in this ensemble (cf. section 3).

Another set of the ensemble is made with the full GCM (MIROC5 PPE-C; "C" stands for the coupled model). With a reduced set of 10 parameters, 5000 perturbation samples are generated using the Latin hypercube sampling technique. In order to avoid climate drift, the N samples with the smallest radiative imbalance at TOA, estimated using a linear emulator of the MIROC5 PPE-A, are selected. The above requirement enssures that the global-mean SAT is not significantly different from the standard experiment without observational constraints unlike MIROC3 PPE-S. We set N = 35, and the 30 y control integration (initial 10 y is the spin-up period and is excluded from the analysis) and 20 y abrupt 4×CO_2 runs are carried out for each member. The radiative forcing and feedback are then calculated using the difference in annual-mean fields between the two runs, following Gregory et al. (2004).

c. MIROC5 MPE

In generating the MPE, we use the T42L40 atmosphere component of MIROC5 as a base model. The parameterization schemes for three processes in MIROC5—cumulus convection, large-scale condensation (LSC) and cloud physics, and turbulence—are reverted to those in MIROC3.2. References and major properties of the schemes are summarized in Table 1. Briefly, each of the schemes implemented in MIROC5 has a greater number of degrees of freedom (e.g., time-dependent entrainment profile in cumuli, explicit treatment of cloud liquid and ice, prognostic turbulent kinetic energy). Unlike some GCMs, we have not implemented a specific scheme for shallow cumulus clouds, but the new convection scheme in MIROC5 is expected to represent these to some extent (Chikira and Sugiyama 2010). The atmosphere model of MIROC5 is different from that of MIROC3.2 in respects of some other physical processes. For example, an updated radiation code calculates the radiative heating more accurately, and the aerosol module was upgraded to include a prognostic scheme for determining the cloud droplet and ice crystal number concentrations, which are important for the indirect aerosol effect (see Watanabe et al. 2010 for details). However, we restrict our attention to the cloud-radiative interaction in this study, so do not change these schemes.

The resulting ensemble is called MIROC5 MPE-A, and consists of eight slightly different models (see Table 2), including the standard MIROC5 (STD). The abbreviations CLD, CUM, and VDF indicate that the cloud (LSC and microphysics), cumulus, and turbulence schemes are replaced by the corresponding old routines. When two of these schemes are replaced, the model is denoted as CLD+CUM, CUM+VDF, or CLD+VDF. The model CLD+CUM+VDF, in which all three schemes have been reverted, is the closest to MIROC3.2 in terms of the representation of cloud-related processes. Since the above procedure often results in a large radiative imbalance at the TOA, we re-tuned each model by slightly modifying a few parameters among the 13 and 10 control parameters in MIROC3 PPE-S and MIROC5 PPE-C, respectively, in order to obtain a radiatively balanced climate (allowable imbalance is ±2 W m^{-2}). The radiative forcing and feedback are evaluated in a similar manner to MIROC5 PPE-A, using the atmosphere-only integration.

3. Climate sensitivity

As a prelude to a more in-depth look at the MIROC5 MPE-A, the ECS of various ensembles is compared in this section. Recall that the definition of ECS ($\Delta T_{2\times}$) is given by the global-mean energy equation

$$\Delta F + \alpha \Delta T_{2\times} = 0 \ , \qquad (1)$$

where ΔF denotes the change in the net TOA radiation when doubling the CO_2 level (positive value means heating the system), and α is the total feedback parameter in W m^{-2} K^{-1}. In atmospheric GCM (AGCM) experiments such as our MPE, these quantities are obtained from the time-mean differences in F between the control and CO_2 runs and between the control and SST runs divided by the global-mean SAT difference. ECS is then estimated using (1).

ECS in the standard version of MIROC3.2 is relatively high in the range obtained from the CMIP3 ensemble (2.5-6.3 K, following Gregory and Webb 2008). This results in MIROC3 PPE-S yielding an ECS range of 4.5-9.6 K (Table 3). In contrast, MIROC5 PPE-A and PPE-C have smaller ECS spreads: 2.3-3.1 K and 2.2-2.7 K, respectively. Even though these produce a comparable spread of radiative forcing and feedback to MIROC3 PPE-S, the ECS is proportional to α^{-1} and hence the MIROC5 PPEs based on a low-sensitivity base model underrepresent the spread of ECS. The fact that the ECS ranges of the MIROC3 PPE-S and MIROC5 PPEs do not overlap (cf. Table 3) indicates that the structural differences between the two base models are greater than the uncertainty range due to model parameters. It is anticipated that the MPE will fill this gap.

Table 2 shows ECSs of individual models in MIROC5 MPE-A. The value of STD is within a range of ECS in MIROC5 PPE-A, but the values from other models are all equal to or larger than this. As expected, the ECS of CLD+CUM+VDF is the highest, at 5.9 K, which is above the range of the MIROC5 PPEs but within that of MIROC3 PPE-S.

ECSs of the various ensembles are plotted as a function of the radiative forcing and the total climate feedback in Fig. 2, on which isolines of $\Delta T_{2\times}$ for a given ΔF and α are also imposed. As has been documented in Tables 2 and 3, ECSs in MIROC3 PPE-S are at the high end while those in MIROC5 PPEs are at the low end (green and red symbols, respectively) compared with the scattering of the CMIP3 MME. It is evident from Fig. 2 that the above difference is attributable to a different magnitude of the total feedback, but not the radiative forcing. The spreads in ΔF and α in MIROC3 PPE-S and MIROC5 PPE-C are narrower than those in CMIP3 MME, but wider than in MIROC5 PPE-A. As expected, the MPE-A fills the gap between MIROC3 PPE-S and the MIROC5 PPEs, despite the fact that ΔF and α are somewhat different from one another. It is intriguing that ΔF and α are negatively correlated within the respective ensembles of MIROC3 PPE-S and MIROC5 PPE-C, which has been pointed out by Shiogama et al. (2011).

Forcing and feedback associated with individual components of the radiative fluxes (not shown) reveal that the primary component responsible for the different ECS in MIROC5 MPE-A is the cloud-shortwave feedback, ΔSW_{cld}. This is clearly seen from a scatter diagram of ECS and ΔSW_{cld} for eight models (Fig. 3, marked by "X"). The correlation between the two quantities reaches 0.85, with the highest value of ΔSW_{cld} in CLD+CUM+VDF. When ΔSW_{cld} is decomposed into tropical (30º S-30º N) and extratropical (30º -90º S and 30º -90º N) components, the latter (square) is always negative and does not differ much among the models, whereas the former (triangle) is highly correlated with ECS as in the global-mean, suggesting the dominant role of the tropical cloud response. In contrast to the negative ΔSW_{cld} in STD (-0.31 W m^{-2}), two models (CLD+VDF and CLD+CUM) show positive values of ΔSW_{cld} (0.53 and 0.20 W m^{-2}, respectively) close to that of the CLD+CUM+VDF model (0.56 W m^{-2}). Since ΔSW_{cld} is weakly positive in CLD and CUM but nearly neutral in VDF, the effect of coupling between two processes is nonlinear. It is thus likely that the major source of diversity in ΔSW_{cld} is a coupling between sub-grid scale processes, rather than one single process. This argument is consistent with the conclusion of Zhang and Bretherton (2008), who used a multi-physics SCM to examine the cloud feedback in CAM.

The horizontal distribution of ΔSW_{cld} is compared among eight models in Fig. 4, from which we identify the following differences. The old cloud scheme in CLD does not modify the overall pattern of ΔSW_{cld}, but strengthens the positive feedback over the subtropical oceans and tropical continents (Fig. 4b). The replacement of the convection scheme (CUM) changes the sign of ΔSW_{cld} (from negative to positive) over the convective regions, as represented by contours of the 500 hPa vertical *p*-velocity (ω) (Fig. 4c). The different turbulence scheme in VDF appears to have little effect on ΔSW_{cld} (Fig. 4d). The effects of these individual schemes persist when we couple them (Fig. 4e-h). However, as seen in Fig. 3, the coupling effect of these processes does not work additively, and hence suppresses or amplifies the regional change in ΔSW_{cld}.

Before conducting a thorough analysis of the dependence of ΔSW_{cld} on the circulation regime in the next section, we can look at the relative contribution of ΔSW_{cld} in different regimes (Fig. 5). By referring to ω, every grid over 30º S-30º N is classified into one of four regimes: strong subsidence ($\omega > 30$ hPa dy^{-1}), weak subsidence ($0 < \omega < 30$), weak ascent ($-40 < \omega < 0$), and strong ascent ($\omega < -40$ hPa dy^{-1}). It is shown in Fig. 5 that ΔSW_{cld} is positive in the subsidence regime of all the models, despite the different magnitudes. However, ΔSW_{cld} in the convective (i.e., ascent) regimes is positive in some models and negative in others. Because the weak subsidence regime occurs the most frequently (Fig. 5b), the positive ΔSW_{cld} in this regime will dominate, as emphasized in previous studies (e.g., Bony and Dufresne 2005). Nevertheless, the sign of ΔSW_{cld} in this regime does not change in the MIROC5 MPE-A. This is consistent with the finding of Watanabe et al. (2011b), who showed that low clouds decrease for the 4×CO_2 case in both MIROC3.2 and MIROC5. The different sign of the tropical-mean ΔSW_{cld} in the MPE-A (Fig. 3) thus comes from diversity in the weak ascent regime, in addition to the different magnitude of positive ΔSW_{cld} in subsidence regimes.

4. Regime analysis for the cloud and cloud shortwave feedback

a. Regime dependence of cloud response and ΔSW_{cld}

It has been shown that ΔSW_{cld} in many GCMs is primarily due to thermodynamic changes in clouds but not changes in the dynamical condition that is represented by the probability density function (PDF) of ω (Bony et al. 2004). Therefore, we made composites of ΔSW_{cld} and the associated changes in high-, mid-, and low-cloud (ΔC_h,

ΔC_m, and ΔC_l) with respect to ω over 30º S-30º N. The width of the ω-bin is 5 hPa dy^{-1}, and the composites for the eight models in MIROC5 MPE-A are plotted together in Fig. 6.

Unlike the CMIP3 MME (cf. Bony and Dufresne 2005), the spread of ΔSW_{cld} is large for both the convective ($\omega < 0$) and subsidence ($\omega > 0$) regimes (Fig. 6a). All of the models show a positive ΔSW_{cld} over the subsidence regions, whereas it is both positive and negative over the convective regions. There is a contrast in the diversity of cloud amounts between the middle/high level and low level—the former has a large spread over the convective regime and the latter varies more over the subsidence regime (Fig. 6b-d). A careful comparison of the ΔSW_{cld} composite and the cloud changes reveals that the cloud-shortwave feedback in different circulation regimes is associated with the cloud change at different altitudes. For example, ΔSW_{cld} is strongly positive in CLD+VDF over the subsidence regime, where ΔC_l is remarkably negative (red lines in Fig. 6a,d). Also, two models (CLD+CUM and CLD+CUM+VDF) show a positive ΔSW_{cld} over the convective regime accompanied by a reduction in C_m (Fig. 6a,c). In CLD+CUM+VDF, ΔC_h is also negative, which might contribute to an amplification of ΔSW_{cld} .

As can been seen in Fig. 4, the cloud-shortwave feedback to ocean surface warming related to an increase in atmospheric CO_2 occurs not only over the subtropical cool oceans, but also over the entire tropics. Thus, the variety in ΔSW_{cld} cannot be explained solely by the change in low-level clouds. Indeed, Fig. 6 illustrates that ΔSW_{cld} is associated with the change in mid-level clouds over the convective regime. In the next section, we extend our regime analysis to examine changes in the vertical structure of clouds and their mechanisms.

b. Analysis using the saturation excess

Observations show that the spatial pattern and seasonal cycle of the subtropical C_l are closely related to the inversion strength above the planetary boundary layer (PBL), as measured by lower-tropospheric stability (LTS) or its variant of the Estimated Inversion Strength (Klein and Hartmann 1993; Wood and Bretherton 2006). Previous studies applied this empirical relationship to interpret the response of C_l to global warming in GCMs (e.g., Wyant et al. 2009; Medeiros and Stevens 2011; Watanabe et al. 2011b). However, LTS cannot be used to diagnose the change in the vertical profile of clouds. We therefore use a different in-situ variable, which is more directly related to warm-phase cloud generation and dissipation in the model.

In a LSC scheme assuming a PDF of sub-grid scale liquid temperature (T_l) and total water (q_t), cloud fraction (C) is calculated by referring to the grid-scale saturation excess (Q_c) and the higher PDF moments (μ_i) as

$$C = f\left(Q_c, \mu_i\right) \ , \qquad (2)$$

where f is a nonlinear function depending on the base distribution of the PDF. The saturation excess is defined as

$$Q_c = a_L \left\{q_t - q_s(T_l, p)\right\} \ , \qquad (3)$$

where p is pressure, q_t the grid-scale total water, q_s the saturation specific humidity, and

$$a_L = \left(1 + L\alpha_L / c_p\right)^{-1} \ , \quad \alpha_L = \partial q_s / \partial T\big|_{T=T_l} \ .$$

An example of the Q_c-C relationship is presented in Fig. 7, which shows a scatterplot of monthly C against Q_c in the tropical lower troposphere from STD (η =

0.88; η is the model's hybrid σ-p coordinate). As C also depends on the PDF moments, and is modified by other microphysical processes during a model time step, the scatter is not exactly fitted by the theoretical curve expected from the LSC scheme. Yet, Fig. 7 shows that Q_c provides a good measure for C, not only in terms of the spatial pattern but for temporal variability (not shown). The gradient of $\partial C / \partial Q_c$ differs somewhat between the LSC schemes used in MIROC3 and 5, but this does not seriously affect the present analysis.

Particularly large changes occur in two models of CLD+VDF and CLD+CUM, with respect to STD (Figs. 3 and 6), and so regime composites of C and Q_c from these three models are compared, focusing on their vertical profiles (Fig. 8). The composite of the cloud fraction in the respective control runs generally shows middle and high clouds over the convective regime and low clouds over the subsidence regime (Fig. 8a,d,g). A salient feature in STD is the coexistence of the three types of cloud at $\omega < 0$: high cloud at around $\eta = 0.2$, middle cloud at $\eta = 0.6$-0.7, and low cloud above $\eta = 0.8$ (Fig. 8a). These are consistent with the observed trimodal structure of cumulonimbus, cumulus congestus, and shallow cumulus (Johnson et al. 1999), although C_l is somewhat overrepresented. In CLD+VDF, high clouds are exaggerated and low clouds form near the surface, particularly in the subsidence regime (Fig. 8d). These changes from STD are caused by the old turbulence scheme, which tends to simulate shallow PBL, and the old cloud scheme, which does not implement cold rain microphysics and thereby overestimates ice clouds (Watanabe et al. 2010). In CLD+CUM, the overall cloud structure is similar to that in CLD+VDF, but lacks a sharp cumulus congestus peak and shallow cumulus in the convective regime (Fig. 8g). It has been confirmed that the standard cumulus scheme in MIROC5 generates more congestus and shallow cumulus than the old scheme (Chikira and Sugiyama 2010). Due to a lack of observations, we cannot verify which cloud structure is the most realistic among the three models, but the mean C_l, C_m, and C_h in STD are found to resemble satellite observations (see section 5).

The change in the cloud fraction (ΔC) in STD is shown in Fig. 8b (shading) imposed on the contour of the mean cloud fraction. As commonly found in global warming experiments, deep cumulus clouds (both congestus and cumulonimbus) are shifted to higher altitudes due to the increased moist adiabatic temperature profile. The shift results in an increase and decrease of cloud above and below the mean position, respectively, without large changes in C_h and C_m due to their cancellation (cf. Fig. 6b,c). However, low cloud is increased over the convective regime. The changes in C are well measured by the change in Q_c, except for the ice cloud at $\eta < 0.2$ (Fig. 8c). The mechanism of the change in Q_c is examined further later in this section.

The composite of ΔC in CLD+VDF is similar to that in STD, except for a stronger contrast between positive and negative changes and an opposite sign at low levels (Fig. 8e). This is reasonable, because ΔSW_{cld} is different between the two models due to the opposite sign of ΔC_l (Fig. 6). It is worth noting that the composites of ΔQ_c from STD and CLD+VDF have a similar structure, even at low levels (Fig. 8f). Namely, ΔQ_c is positive at η = 0.8-0.9 over the convective regime and negative at $\eta > 0.8$ over the subsidence regime. In STD, the positive low-level ΔQ_c occurs where clouds exist in the control run, and therefore serves to increase C. In CLD+VDF, however, clouds form in the control run beneath the level of the positive ΔQ_c. Because of the small $\partial C / \partial Q_c$ in the unsaturated condition (Fig. 7), ΔQ_c cannot act to amplify the low clouds at η = 0.8-0.9.

Similarly, the variation in ΔC where $\omega > 0$, which is close to zero in STD but negative in CLD+VDF, can be explained by the difference in the peak altitude of the mean clouds. The negative ΔQ_c in the lower troposphere at $\omega > 0$ is not uniform, being larger near the surface and where $\eta < 0.8$ (Fig. 8c,f). The mean cloud, i.e., climatology in the control run, in CLD+VDF is generated at $\eta > 0.9$, where ΔQ_c is large. This causes the cloud reduction to occur. The difference in altitude of the mean cloud in STD and CLD+VDF is associated with the different PBL depth, which tends to be thinner when the lower order turbulence closure is used. In summary, our comparison of ΔC and ΔQ_c between STD and CLD+VDF indicates that the mean cloud structure, and whether it is formed at the height where ΔQ_c works effectively, is the key to the opposite ΔC_l (and hence ΔSW_{cld}) behavior.

In CLD+CUM, as in the other models, high clouds are shifted upward (Fig. 8h). As the control run lacks low cloud over the convective regime (Fig. 8g), this does not change in response to the positive Q_c (Fig. 8i). A major difference from STD (and also CLD+VDF) is the change in the middle cloud, which shows a marked decrease at η = 0.6-0.7. The middle cloud tends to decline at the peak altitude of mean cloud in all the models. The middle clouds are much broader in CLD+CUM than in the other two models, and their decrease is not compensated by an increase in the upper levels at around $\eta = 0.45$. ΔC_m takes its largest negative value in this model (Fig. 6h), which explains the strong positive ΔSW_{cld} over the convective regime. It is thus likely that the response of the cumulus congestus is different between models adopting different convection schemes, which is another crucial factor in the diversity of ΔSW_{cld}.

Since the structure of ΔQ_c is similar in each of the models, unlike ΔC (see Fig. 8), the mechanisms of ΔQ_c are further examined. Using (3), ΔQ_c can be expressed as

$$\begin{aligned}\Delta Q_c &= \bar{a}_L\left(\Delta q_t - \Delta q_s\right) + \Delta a_L\left(\bar{q}_t - \bar{q}_s\right) \\ &= \bar{a}_L\left[(\bar{H}-1)\bar{\alpha}_L\Delta T + \Delta H\bar{q}_s + \left\{1-(\bar{H}-1)\bar{\alpha}_L L/c_p\right\}\Delta q_l\right] + \Delta a_L\left(\bar{q}_t - \bar{q}_s\right)\end{aligned} \tag{4}$$

where H denotes relative humidity (RH), and q_l is the cloud water. The overbar and Δ indicate values from the control run and the difference between the control and SST runs, respectively. Following the decomposition in (4), ΔQ_c may be explained by four effects, corresponding to each term in the rhs of the second equation: a temperature effect, a RH effect, a condensate effect, and the Clausius-Clapeyron (CC) effect. The CC effect works through a reduction in α_{L} with increasing T_l, and vice versa.

In order to examine the reasons for positive ΔQ_c where $\omega < 0$ and negative ΔQ_c where $\omega > 0$ commonly found in the lower troposphere (Fig. 8c,f,i), regime composites of the above terms are calculated. Figure 9 presents three of these terms, and their sum, from STD. The condensate effect is found to be negligible, and hence, is not shown. In response to the ocean surface warming, radiative cooling in the free troposphere is known to strengthen over the subsidence region (Zhang and Bretherton 2008; Wyant et al. 2009, Brient and Bony 2011). The enhanced clear-sky longwave cooling is associated with the tropospheric warming, which works to reduce Q_c (Fig. 9a). The negative temperature effect is similarly found near the surface due to increased sensible heat. The CC effect, which comes from nonlinearity in the Clausius-Clapeyron relationship, is roughly the opposite of the temperature effect (Fig. 9b), although weaker in magnitude. The sum of the above two effects is dominated by the temperature effect, and shows a uniform negative contribution to Q_c in the PBL (not shown).

Unlike the other terms, the RH effect has positive and negative values in the PBL at $\omega < 0$ and $\omega > 0$, respectively (Fig. 9c). This contrast is reflected in the sum of the three terms (Fig. 9d), which well reproduces the actual structure of ΔQ_c (cf. Fig. 8c). Considering that ΔH can be decomposed into $\Delta H \doteq \left(\Delta q \overline{q}_s - \overline{q}\Delta q_s\right)/\,\overline{q}_s^{\,2}$, the positive contribution indicates that the moisture increase is greater than the increase in saturation humidity, and vice versa for the negative contribution. The RH effect seen in the middle level corresponds to the upward shift of clouds, in addition to an enhanced cloud re-evaporation at $\eta = 0.55$, which has been confirmed from the composites of the water vapor and cloud water tendency terms (not shown). There is a theoretical study that supports robust free-tropospheric RH in global warming (Sherwood and Meyer 2006), but the RH change responsible for Fig. 8c is small: about 2% in the PBL and 8% in the middle troposphere. These changes are allowable in theory, but may be sufficient to change the cloud property.

5. Possible constraint to the cloud-shortwave feedback

The results of the analysis presented in the previous section highlight the active role played by the changes in C_l and C_m over the convective regime, and the change in C_l over the subsidence regime, in understanding ΔSW_{cld}. In this section, we again use the models available in the MPE to identify a more generalized relationship in the ensemble.

Figure 10 shows a scatter diagram of ΔSW_{cld} against both $\Delta C_l + \Delta C_m$ and ΔC_l, according to the circulation regime. The condition of weak ω may be a mixture between the convective and subsidence regimes, but we simply use a threshold of $\omega = 0$ to partition the two regimes in Fig. 10. The composite is also plotted for MIROC3 PPE-S and MIROC5 PPE-A, but not for MIROC5 PPE-C because the regional change in this ensemble is contaminated by the natural variability arising from a full atmosphere-ocean coupling.

Overall, ΔSW_{cld} is negatively correlated with the cloud changes in both regimes; it is not surprising because more cloud will reflect more shortwave radiation and vice versa. This negative relationship is even found in each ensemble, with the exception of the MIROC5 PPE-A over the subsidence regime, where ΔSW_{cld} and ΔC_l remain almost unchanged (red circles in Fig. 10b). With the MIROC5 MPE-A, we obtain estimates of -1.4 and -1.2 W m^{-2} decrease of SW_{cld} per 1% increase of $C_l + C_m$ and C_l over the convective and subsidence regimes, respectively. These estimates do not change much when we use two PPEs together. It is interesting to note that ΔSW_{cld} is positive in most cases, indicating an additional process that contributes to solar insolation without changes in the cloud amount. A possible explanation for this is the so-called cloud masking effect (Soden et al. 2004), which occurs due to the different sensitivity of clear- and cloudy-sky shortwave radiation to changes in water vapor and albedo, but not cloud fraction.

Given a crude linear dependence of ΔSW_{cld} upon either ΔC_l+ΔC_m or ΔC_l, we intuitively assume that there is a systematic relationship between the mean cloud states and their change, and hence ΔSW_{cld} (e.g., Yokohata et al. 2011). In order to confirm this idea, scatter diagrams are produced of the regime-sorted ΔSW_{cld} against mean cloud amounts, $\bar{C}_l + \bar{C}_m$ and $\bar{C}_l$, over the respective regime obtained from the annual-mean climatology in the control runs (Fig. 11). The mean cloud amounts can be compared with the ISCCP data (Rossow and Schiffer 1999), which are imposed on Fig. 11 by thick vertical lines with grey shading to indicate the range of the interannual variability for 1984-2007.

Over the convective regime, MIROC5 MPE-A fills the gap between two PPEs, one showing less $\bar{C}_l + \bar{C}_m$ and larger ΔSW_{cld} (MIROC3 PPE-S) and the other with more $\bar{C}_l + \bar{C}_m$ and near-neutral ΔSW_{cld} (MIROC5 PPE-A) (Fig. 11a). The dependence of ΔSW_{cld} on $\bar{C}_l + \bar{C}_m$ in MPE is not monotonic, but has a peak at $\bar{C}_l + \bar{C}_m \sim 30\%$. Possible reasons for the ΔSW_{cld} dependence on $\bar{C}_l + \bar{C}_m$, as approximated by a second-order polynomial (black curve in Fig. 11a) are as follows. As identified in Fig. 8, the sign and magnitude of ΔC_m are related to the sharpness of $\bar{C}_m$, which is not easily measurable. Instead, we use $\bar{C}_m$ itself, which will be proportional to the sharpness of $\bar{C}_m$. The negative slope for $\bar{C}_l + \bar{C}_m$ > 30% is therefore interpreted to imply that less mean cloud (i.e., a less sharp vertical structure) accompanies the net decrease rather than the upward shift of C_m, and hence the positive ΔSW_{cld} (cf. Fig. 8). This effect will be saturated or even diminished when $\bar{C}_m$ is too small. The contribution of ΔC_l is of secondary importance over the convective regime, where ΔQ_c is positive and hence ΔSW_{cld} tends to be negative due to ΔC_l; this occurs when $\bar{C}_l$ is sufficient at levels where ΔQ_c is large (η = 0.8-0.9, Fig. 8). In summary, a model generating more $\bar{C}_l + \bar{C}_m$ will have ΔSW_{cld} close to neutral due to cancellation between positive ΔC_l and negative ΔC_m. The decrease in C_m prevails over the increase in C_l for moderate amounts of $\bar{C}_l + \bar{C}_m$, but will diminish for much less $\bar{C}_l + \bar{C}_m$. This results in the nonlinear dependence of ΔSW_{cld} on the mean clouds, with the maximum value of ΔSW_{cld} occurring somewhere in the middle. While the validity of the curve estimated from MIROC5 MPE-A for the MME is not assured, an intersection of the extrapolated curve with the mean cloud obtained from ISCCP suggests that a near-neutral or weakly negative ΔSW_{cld} is plausible over the convective regime.

Likewise, the sensitivity of ΔSW_{cld} to the mean low cloud over the subsidence regime is nonlinear (Fig. 11b). Again, ΔSW_{cld} is positive with less $\bar{C}_l$ (< 20%) in MIROC3 PPE-S, whereas MIROC5 PPE-A shows a nearly neutral ΔSW_{cld} with $\bar{C}_l \sim 30\%$, having a small spread. All the MPE models exhibit positive ΔSW_{cld}, with the minimum values occurring in models with a moderate amount of $\bar{C}_l$. Over the subsidence regime, $\bar{C}_l$ is roughly proportional to the mean PBL depth in MPE (not shown, but the PBL height varies from 950 to 1200 m among the eight models). The inversion strength is larger with deeper PBL, so that this proportionality will be reasonable. As seen in Fig. 8c,f,i, however, negative ΔQ_c is not uniform in the PBL but is larger near the surface and the free troposphere. Thus, models generating clouds at too low ($\eta > 0.9$) or too high ($\eta \sim 0.8$) levels are likely to show a greater decrease in C_l. A comparison of $\bar{C}_l$ with the ISCCP climatology suggests that a model showing a weak positive feedback is plausible, which corresponds to $\bar{C}_l$ being generated at around $\eta = 0.85$. For further constraints, validation of the PBL height, and the dominant processes that control the height, will be desirable (Medeiros et al. 2005).

6. Concluding discussion

In this study, we constructed a model ensemble in which each of eight atmospheric models is structurally different. The differences were systematically formed by replacing one or more parameterization schemes for the atmospheric processes, i.e., cumulus convection, cloud, and turbulence, between two versions of MIROC. This ensemble, called MIROC5 MPE-A in the present paper, was made by reverting the respective scheme in a newer version of MIROC5 with the scheme used in the previous version of MIROC3.2. The MIROC5 MPE-A enabled us to connect two base models showing opposite cloud-shortwave feedback, ΔSW_{cld}, to global warming, and was used to explore the cause of diversity in ΔSW_{cld} in the IPCC-class GCMs.

Climate change simulations were carried out using the MIROC5 MPE-A, by either quadrupling CO_2 or increasing SST, in order to obtain the radiative forcing and the climate feedback, both of which are necessary to estimate equilibrium climate sensitivity, ECS. MIROC5 MPE-A showed an ECS range of 2.3-5.9 K, which is as wide as that in the CMIP3 MME and MIROC3.2 PPE, and wider than the range obtained from MIROC5 PPE. As in the many IPCC-class models, the difference in the tropical ΔSW_{cld} is the major driver for the wide range of ECS in MIROC5 MPE-A.

Causes of the tropical ΔSW_{cld} and associated cloud changes were examined by referring to the circulation regimes. It was found that the tropical ΔSW_{cld} is not controlled by any single process, but rather by the coupling of two processes. The mean and the response of low clouds over the subsidence regime were greatly altered in the model with changed cloud and turbulence schemes, whereas low and middle clouds over the convective regime were affected by replacing the convection and cloud schemes. Both of the coupled processes act to enhance the positive ΔSW_{cld}, which was found in MIROC3.2 but not in MIROC5. While the details of how the processes are coupled when modifying the cloud behavior were not fully clear, the resultant mean vertical structure of clouds in the control simulation was different among the models, which often generated opposite signs of the cloud response to a robust change in the thermodynamic field, as represented by Q_c (section 4). For each of the circulation regimes, ΔSW_{cld} and cloud changes in MPE had a nonlinear, but systematic, relationship with the mean cloud amount, which may be constrained using satellite estimates. The analysis suggests a weak positive feedback over the subsidence regime and a near-neutral or weak negative ΔSW_{cld} over the convective regime (section 5).

It will be essential to evaluate the processes controlling the cloud response to global warming in order to understand the diversity in ΔSW_{cld}. The C_l change in MPE can be both positive and negative over the subsidence regime (Fig. 10b), which may aid further understanding of why C_l increases in some models and decreases in others. Possible key parameters are the change in the PBL height and the PBL wetness. If the PBL gets thicker due to destabilization with increasing SST, this will work to increase low clouds (Xu et al. 2010). The PBL can also be thinner, and hence C_l decreases, if the cloud-top entrainment is weakened for any reason (Lauer et al. 2010). Such changes in the PBL depth appear to occur in fine resolution models that resolve a subtle change in the inversion height. The PBL height in MPE changes by about ± 10 m, which is much less than the change found in Lauer et al. (2010). Another factor, the PBL wetness change, is determined by a balance between the increased moisture sources from surface evaporation and the altered advection of dry air from the free troposphere (Wyant et al. 2009; Brient and Bony 2011). In the MIROC5 MPE-A, the PBL over the subsidence regime became drier when the ocean warmed, which supports the positive low-cloud feedback. However, we further identified that the magnitude of ΔSW_{cld} varies depending on the mean C_l and the PBL height because the change in the saturation excess is not uniform within the PBL.

Because the strong subsidence regime occupies a small area in the tropics (cf. Fig. 5), some recent studies have emphasized the importance of the change in shallow cumulus cloud that occurs for weak ω (Medeiros et al. 2008; Gettelman et al, 2011). While many studies examined the feedback associated with shallow cumulus over the weak subsidence regime, the cloud composite shown in Fig. 8 clearly indicates that the shallow convective clouds are smoothly extended to the convective regime, where the cumulus congestus and cumulonimbus sometimes overlap. It is therefore reasonable that ΔSW_{cld} over the convective regime changed the most when the cumulus convection scheme in STD was replaced (i.e., CLD+CUM). One of our conclusions, that the change in the middle cloud representing cumulus congestus is also a crucial factor for different ΔSW_{cld} among the models, has not been pointed out so far. This may be partly due to all the CMIP3 models underrepresenting cumulus congestus, and thus its importance for cloud-shortwave feedback. We might expect the updated models in CMIP5 to show a higher sensitivity of ΔSW_{cld} to cumulus congestus, as in MIROC5.

We have demonstrated that our MPE has advantages over a PPE in understanding sources of different cloud feedbacks in GCMs. Yet the MPE has a similar limitation to PPEs in a qualitative sense. Namely, the diversity in the ensemble crucially depends on the two base models that are to be connected by the MPE. For example, we tried to constrain ΔSW_{cld} by using the mean cloud amount in Fig. 11, which may have a different curve between ΔSW_{cld} and either $\bar{C}_l + \bar{C}_m$ or $\bar{C}_l$ when the base models are different. In this regard, the constrained ΔSW_{cld} for the convective and subsidence regimes may still be tentative. Ideally, a MPE based on multiple GCMs will eventually fill the gaps among structurally different GCMs in the CMIP3 MME. In reality, such modeling is not possible unless a coordinated collaboration between the modeling centers is established. In practice, an examination of the relationship between ΔSW_{cld}

and the mean cloud properties using the CMIP5 database, which is currently under preparation and will soon be available, should be the primary aim of future work.

Acknowledgments

This work was supported by the Innovative Program of Climate Change Projection for the 21st Century ("Kakushin" program), Grant-in-Aid 23310014 and 23340137 from MEXT, Japan, and by the Mitsui & Co., Ltd., Environment Fund C-042. The computation was carried out on the Earth Simulator, NEC SX at NIES, and HITACHI HA8000 at the University of Tokyo.

REFERENCES

Annan, J. D., J. Hargreaves, N. Edwards, and R. Marsh, 2005: Parameter estimation in an intermediate complexity earth system model using an ensemble Kalman filter. *Ocean Modelling*, 8, 135–154.

Bony, S., J.-L. Dufresne, H. LeTreut, J.-J. Morcrette, and C. Senior, 2004: On dynamic and thermodynamic components of cloud changes. *Clim. Dyn.*, 22, 71-86.

Bony, S., and J. L. Dufresne, 2005: Marine boundary layer clouds at the heart of tropical cloud feedback uncertainties in climate models. *Geophys. Res. Lett.*, 32, L20806.

Brient, F., and S. Bony, 2011: Interpretation of the positive low-cloud feedback predicted by a climate model under global warming. *Clim. Dyn.*, submitted.

Chikira, M., and M. Sugiyama, 2010: A cumulus parameterization with state-dependent entrainment rate. Part I: Description and sensitivity to temperature and humidity profiles. *J. Atmos. Sci.*, 67, 2171-2193.

——, 2010: A cumulus parameterization with state-dependent entrainment rate. Part II: Impact on climatology in a general circulation model. *J. Atmos. Sci.*, 67, 2194–2211.

Collins, M., B. B. B. Booth, B. Bhaskaran, G. R. Harris, J. M. Murphy, D. M. Sexton, and M. J. Webb, 2010: Climate model errors, feedbacks and forcings: a comparison of perturbed physics and multi-model ensembles. *Clim. Dyn.*. 36, 1737–1766.

Emori, S., A. Hasegawa, T. Suzuki, and K. Dairaku, 2005: Validation, parameterization dependence and future projection of daily precipitation simulated with a high-resolution atmospheric GCM. *Geophys. Res. Lett.*, **3**, L06708, doi:10.1029/2004GL022306.

Gettelman, A., J. E. Kay, and K. M. Shell, 2011: The evolution of climate sensitivity and climate feedbacks in the Community Atmosphere Model. *J. Climate*, in press.

Gregory, J. M., and Coauthors, 2004: A new method for diagnosing radiative forcing and climate sensitivity. *Geophys. Res. Lett.*, **31**, doi:10.1029/2003GL018747.

——, and M. J. Webb, 2008: Tropospheric adjustment induces a cloud component in CO2 forcing. *J. Climate*, 21, 58–71.

Hargreaves, J. C., A. Abe-Ouchi, and J. D. Annan, 2007: Linking glacial and future climate through an ensemble of GCM simulations. *Climate Past*, 3, 77–87.

Houtekamer, P. L., L. Lefaivre, J. Derome, H. Ritchie, and H. L. Mitchell, 1996: A system simulation approach to ensemble prediction. *Mon. Wea. Rev.*, 124, 1225-1242.

Jackson, L. C., M. Vellinga, and G. R. Harris, 2011: The sensitivity of the meridional overturning circulation to modelling uncertainty in a perturbed physics ensemble without flux adjustment. *Clim. Dyn.*, doi:10.1007/s00382-011-1110-5.

Johnson, R. H., T. M. Rickenbach, S. A. Rutledge, P. E. Ciesielski, and W. H. Schuber, 1999: Trimodal characteristics of tropical convection. *J. Climate*, **12**, 2397-2418.

K-1 Model Developers, 2004: K-1 coupled model (MIROC) description. In: Hasumi H, Emori S (eds) K-1 technical report. 34 pp [available at *http://www.ccsr.u-tokyo.ac.jp/~agcmadm/*].

Klein, S. A., and D. L. Hartmann, 1993: The seasonal cycle of low stratiform clouds. *J. Climate*, 6, 1587-1606.

Klocke, D., R. Pincus, and J. Quaas, 2011: On constraining estimates of climate sensitivity with present-day observations through model weighting. *J. Climate*, 24, doi: 10.1175/2011JCLI4193.1.

Lauer, A., K. Hamilton, Y. Wang, V. T. J. Phillips, and R. Bennartz, 2010: The impact of global warming on marine boundary layer clouds over the eastern Pacific – A regional model study. *J. Climate*, 23, 5844-5863.

Le Treut, H., and Z. X. Li, 1991: Sensitivity of an atmospheric general circulation model to prescribed SST changes: Feedback effects associated with the simulation of cloud optical properties. *Clim. Dyn.*, 5, 175–187.

Medeiros, B., A. Hall, and B. Stevens, 2005: What controls the mean depth of the PBL? *J. Climate*, 18, 3157-3172.

Medeiros, B., B. Stevens, I. M. Held, M. Zhao, D. L. Williamson, J. G. Olson, and C. S. Bretherton, 2008: Aquaplanets, climate sensitivity, and low clouds. *J. Climate*, 21, 4974–4991.

Medeiros, B., and B. Stevens, 2011: Revealing differences in GCM representations of low cloud. *Clim. Dyn.*, 36, 385-399.

Mellor, G. L., and T. Yamada, 1974: A hierarchy of turbulence closure models for planetary boundary layers. *J. Atmos. Sci.*, 31, 1791–1806.

——, and ——, 1982: Development of a turbulence closure model for geophysical fluid problems. *Rev. Geophys. Space Phys*., 20, 851–875.

Nakanishi, M., 2001: Improvement of the Mellor–Yamada turbulence closure model based on large-eddy simulation data. *Bound.-Layer Meteor.*, 99, 349–378.

——, and H. Niino, 2004: An improved Mellor–Yamada level-3 model with condensation physics: Its design and verification. *Bound.-Layer Meteor.*, 112, 1–31.

Murphy, J., D. M. H. Sexton, D. N. Barnett, G. S. Jones, M. J. Webb, M. Collins, and D. A. Stainforth, 2004: Quantification of modelling uncertainties in a large ensemble of climate change simulations. *Nature*, 430, 768–772.

Ogura, T., S. Emori, M. J. Webb, Y. Tsushima, T. Yokohata, A. Abe-Ouchi, and M. Kimoto, 2008: Towards understanding cloud response in atmospheric GCMs: The use of tendency diagnostics. *J. Meteor. Soc. Japan*, 86, 69–79.

Pan, D. M., and D. A. Randall, 1998: A cumulus parameterization with a prognostic closure. *Quart. J. Roy. Met. Soc.*, **124**, 949-981.

Reichler, T., and J. Kim, 2008: How well do coupled models simulate today's climate? *Bull. Amer. Meteor. Soc.*, 89, 303–311.

Rossow,W. B., and R.A. Schiffer, 1999:Advances in understanding clouds from ISCCP. *Bull. Amer. Meteor. Soc.*, 80, 2261–2287.

Sanderson, B. M., K. M. Shell, and W. Ingram, 2010: Climate feedbacks determined using radiative kernels in a multi-thousand member ensemble of AOGCMs. *Clim. Dyn*., 35, 1219–1236.

Sherwood, S. C., and C. L. Meyer, 2006: The general circulation and robust relative humidity. *J. Climate*, 19, 6278-6290.

Shiogama, H., and Coauthors, 2011: Physics parameter ensembles of the MIROC5 coupled-atmosphere-ocean GCM without flux corrections. *Clim. Dyn.*, submitted.

Soden, B. J, A. J. Broccoli, and R. S. Hemler, 2004: On the use of cloud forcing to estimate cloud feedback. *J. Climate*, 17, 3661-3665.

Soden, B. J, and I. M. Held, 2006: An assessment of climate feedbacks in coupled ocean–atmosphere models. *J. Climate*, 19, 3354-3360.

Solomon, S., D. Qin, M. Manning, M. Marquis, K. Averyt, M. M. B. Tignor, H. L. Miller Jr., and Z. Chen, Eds., 2007: *Climate Change 2007: The Physical Science Basis.* Cambridge University Press, 996 pp.

Stainforth, D. A., and Coauthors, 2005: Uncertainty in predictions of the climate response to rising levels of greenhouse gases. *Nature*, 433, 403-406.

Stensrud, D. J., J.-W. Bao, and T. T. Warner, 2000: Using initial condition and model physics perturbations in short-range ensemble simulations of mesoscale convective systems. *Mon. Wea. Rev.*, 128, 2077-2107.

Watanabe, M., S. Emori, M. Satoh, and H. Miura, 2009: A PDF-based hybrid prognostic cloud scheme for general circulation models. *Clim. Dyn.*, 33, 795–816, doi:10.1007/s00382-008-0489-0.

Watanabe, M., and Coauthors, 2010: Improved climate simulation by MIROC5: Mean states, variability, and climate sensitivity. *J. Climate*, 23, 6312-6335.

Watanabe, M., H. Shiogama, T. Yokohata, T. Ogura, M. Yoshimori, S. Emori, and M. Kimoto, 2011a: Constraints to the tropical low-cloud trends in historical climate simulations. *Atmos. Sci. Lett.*, 12, doi:10.1002/asl.337.

Watanabe, M., and Coauthors, 2011b: Fast and slow timescales in the tropical low-cloud response to increasing CO_2 in two climate models. *Clim. Dyn*., in press.

Webb, M. J., and Coauthors, 2006: On the contribution of local feedback mechanisms to the range of climate sensitivity in two GCM ensembles. *Clim. Dyn.*, 27, 17–38.

Wilson, D. R., and S. P. Ballard, 1999: A microphysically based precipitation scheme for the UK Meteorological Office unified model. *Quart. J. Roy. Meteor. Soc.*, 125, 1607–1636

Wood, R., and C. S. Bretherton, 2006: On the relationship between stratiform low cloud cover and lower-tropospheric stability. *J. Climate*, 19, 6425-6432.

Wyant, M. C., C. S. Bretherton, and P. N. Blossey, 2009: Subtropical low cloud response to a warmer climate in a superparameterized climate model. Part I: Regime sorting and physical mechanisms. *J. Adv. Mod. Earth Sys.*, 1, Art. #7, doi: 10.3894/JAMES.2009.1.7.

Xu, K. M., A. Cheng, and M. Zhang, 2010: Cloud-resolving simulation of low-cloud feedback to an increase in sea surface temperature. *J. Atmos. Sci.*, 67, 730-748.

Yokohata, T., M. J. Webb, M. Collins, K. D. Williams, M. Yoshimori, J. C. Hargreaves, and J. D. Annan, 2010: Structural similarities and differences in climate responses to CO_2 increase between two perturbed physics ensembles. *J. Climate*, 23, 1392-1410.

Zhang, M., and C. S. Bretherton, 2008: Mechanisms of low cloud-climate feedback in idealized single-column simulations with the Community Atmospheric Model, version 3 (CAM3). *J. Climate*, 21, 4859-4878.

FIGURE AND TABLE CAPTIONS

Table 1 Description of parameterization schemes used in the two versions of MIROC.

Table 2 Abbreviations for each model of the MIROC5 MPE-A. The ECSs are also shown at the bottom raw.

Table 3 The Range of the ECS in various model ensembles. Values for the CMIP3 ensemble were taken from Gregory and Webb (2008).

Figure 1 Three major approaches for exploring diversity of cloud feedbacks in GCMs. The mark “X” indicates individual CMIP models.

Figure 2 Change in the TOA net radiative forcing, F, and the total climate feedback, α, for various sets of the GCM ensembles: CMIP3 MME (grey circles), MIROC3 PPE-S (green squares), MIROC5 PPE-C (red squares), MIROC5 PPE-A (red “X”), and MIROC5 MPE-A (blue “X”). The isolines of ECS are also indicated. The radiative forcing is scaled to be 2×CO_2 equivalent.

Figure 3 ECS in the MIROC5 MPE-A against the global-mean (“X”), tropical-mean (triangle), and extratropical-mean (square) of the cloud shortwave feedback, ΔSW_{cld}. Each symbol represents the value from a model in MPE-A. The correlation coefficient for each set is indicated at the top-left.

Figure 4 Spatial patterns of ΔSW_{cld} in MIROC5 MPE-A: (a) STD, (b) CLD, (c) CUM, (d) VDF, (e) CLD+CUM, (f) CUM+VDF, (g) CLD+VDF, and (h) CLD+CUM+VDF. The unit is W m^{-2} K^{-1}, and the zero contour of annual-mean ω in the control climate is imposed.

Figure 5 (a) Composite of ΔSW_{cld} over the tropics (30° S-30° N) with respect to four circulation regimes defined by ω. (b) As in (a) but for the regime frequency. Each model in MPE-A is indicated by a dot.

Figure 6 Regime composites of (a) ΔSW_{cld}, (b) ΔC_h, (c) ΔC_m, and (d) ΔC_l over the tropics (30° S-30° N) with respect to ω.

Figure 7 Scatter diagram of C against Q_c at η=0.88 over the tropics in the STD control run.

Figure 8 Regime composite of (a) C, (b) ΔC, and (c) ΔQ_c with respect to ω in STD. Values of C and ω are taken from the control run. Contours in (b)-(c) are the same as shading in (a). (d)-(f) As in (a)-(c) but for CLD+VDF. (g)-(i) As in (a)-(c) but for CLD+CUM.

Figure 9 As in Fig. 8 but for dominant terms to ΔQ_c in STD: (a) temperature effect, (b) CC effect, (c) RH effect, and (d) sum of the three effects. Contours are the C composite in the control run (same as in Fig. 8b).

Figure 10 (a) Scatter diagram of ΔSW_{cld} against ΔC_l+ΔC_m over the convective regime ($\omega < 0$): MIROC3 PPE-S (green circles), MIROC5 PPE-A (red circles), and MIROC5 MPE-A (squares). The error bars for MPE indicate the range of the interannual variability. (b) As in (a) but for ΔSW_{cld} against ΔC_l over the subsidence regime ($\omega > 0$).

Figure 11 As in Fig. 10 but for ΔSW_{cld} against (a) $\overline{C}_l + \overline{C}_m$ for $\omega < 0$ and (b) $\overline{C}_l$ for $\omega > 0$. The thick vertical line with grey shading denotes the mean and the range of the interannual variability derived from ISCCP. Thick curves are the least-square fitted polynomials for the MIROC5 MPE-A.

Table 1 Description of parameterization schemes used in the two versions of MIROC.

	MIROC3.2	MIROC5
cumulus convection	Prognostic AS scheme with triggering function (Pan and Randall 1998; Emori et al. 2005)	Prognostic closure with state-dependent entrainment (Chikira and Sugiyama 2010; Chikira 2010)
cloud (LSC+microphysics)	Diagnostic cloud with simple microphysics (LeTreut and Li 1991; Ogura et al. 2008)	Prognostic cloud with mixed-phase microphysics (Watanabe et al. 2009; Wilson and Ballard 1999)
turbulence	Level 2.0 closure (Mellor and Yamada 1974, 1982)	Level 2.5 closure (Nakanishi 2001; Nakanishi and Niino 2004)

Table 2 Abbreviations for each model of the MIROC5 MPE-A. The ECSs are also shown at the bottom raw.

Model	**STD**	**CLD**	**CUM**	**VDF**	**CLD+ CUM**	**CUM+ VDF**	**CLD+ VDF**	**CLD+ CUM+ VDF**
ECS [K]	2.3	2.5	2.4	2.3	3.0	2.8	4.2	5.9

Table 3 The Range of ECS in various model ensembles. Values for the CMIP3 ensemble were taken from Gregory and Webb (2008).

Ensemble	**CMIP3**	**MIROC3 PPE-S (T21L20, N=32)**	**MIROC5 PPE-C (T42L40, N=35)**	**MIROC5 PPE-A (T42L40, N=42)**
ECS [K]	2.5-6.3	4.5-9.6	2.3-3.1	2.2-2.7

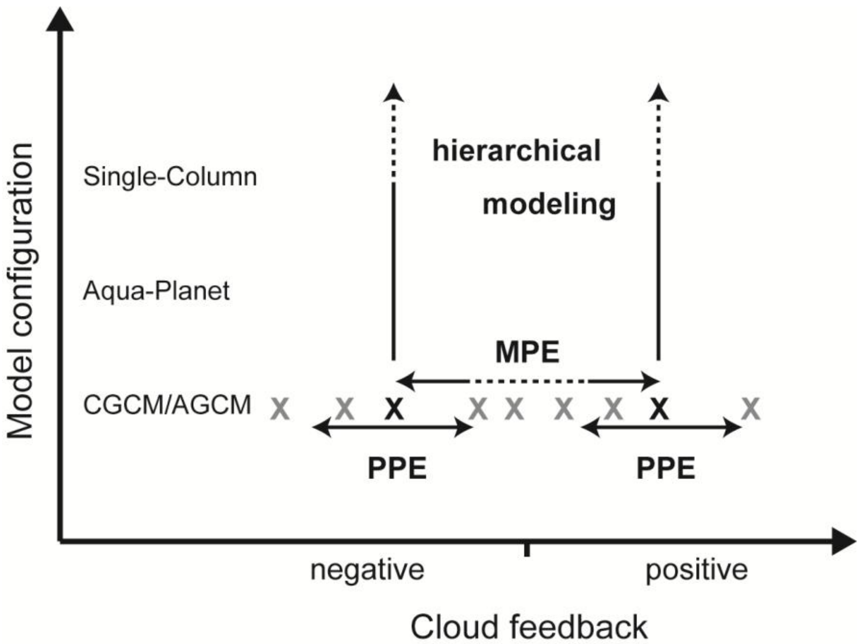

Figure 1 Three major approaches for exploring diversity of cloud feedbacks in GCMs. The mark "X" indicates individual CMIP models.

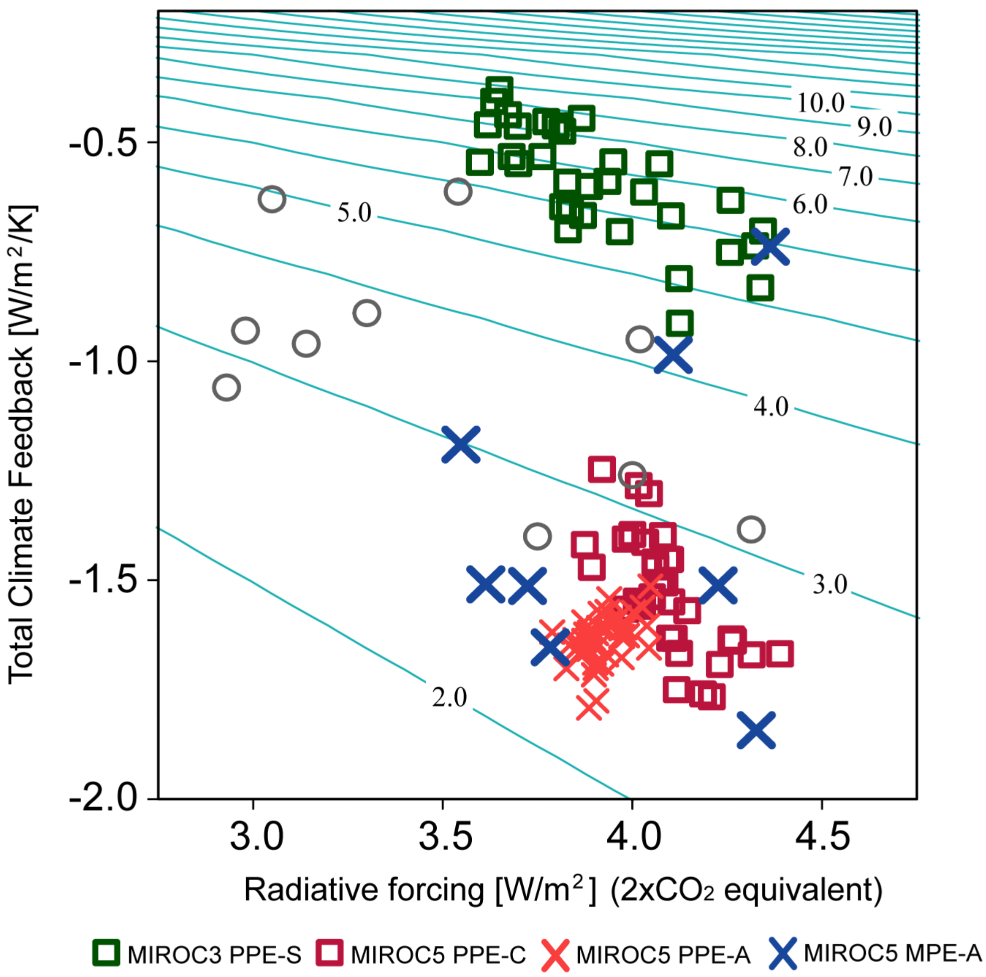

Figure 2 Change in the TOA net radiative forcing, F, and the total climate feedback, α, for various sets of the GCM ensembles: CMIP3 MME (grey circles), MIROC3 PPE-S (green squares), MIROC5 PPE-C (red squares), MIROC5 PPE-A (red "X"), and MIROC5 MPE-A (blue "X"). The isolines of ECS are also indicated. The radiative forcing is scaled to be $2\times CO_2$ equivalent.

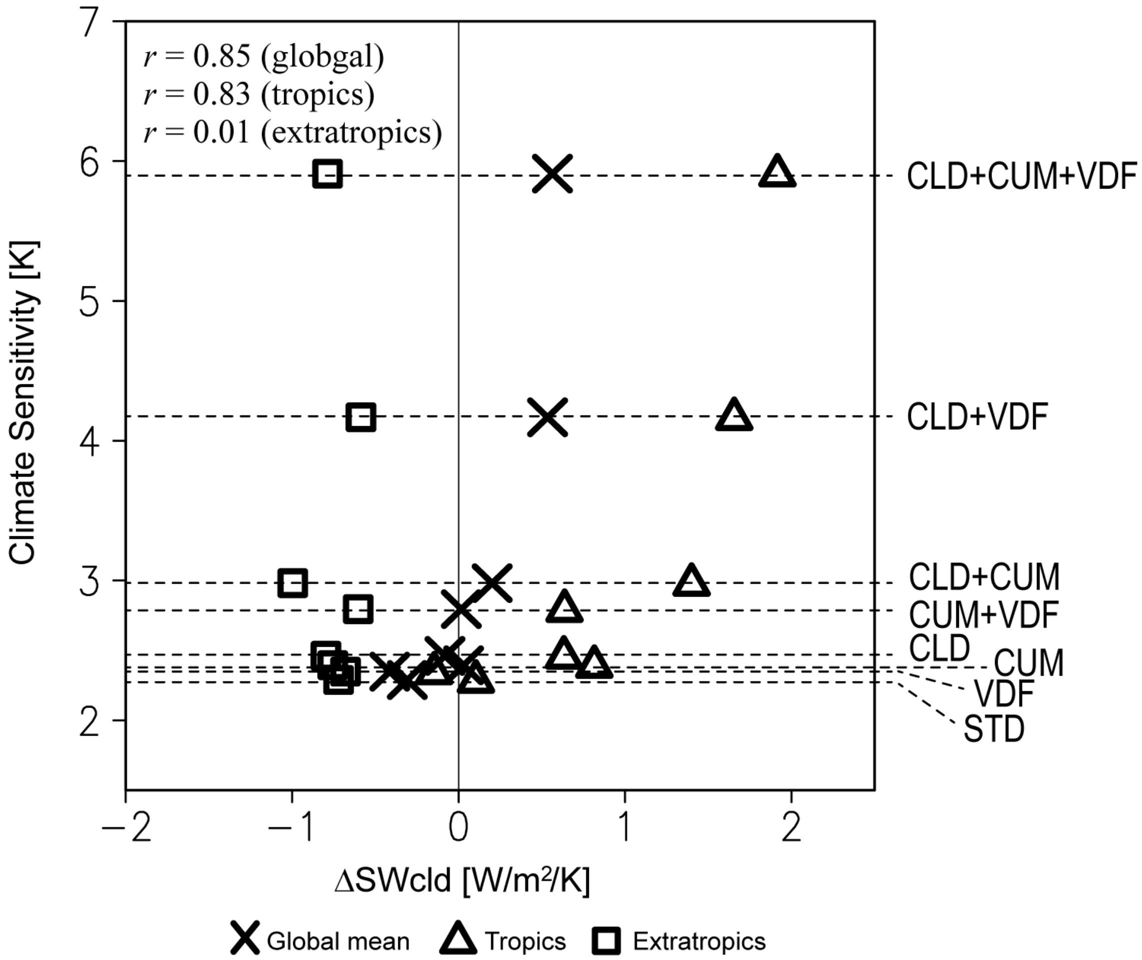

Figure 3 ECS in the MIROC5 MPE-A against the global-mean ("X"), tropical-mean (triangle), and extratropical-mean (square) of the cloud shortwave feedback, ΔSW_{cld}. Each symbol represents the value from a model in MPE-A. The correlation coefficient for each set is indicated at the top-left.

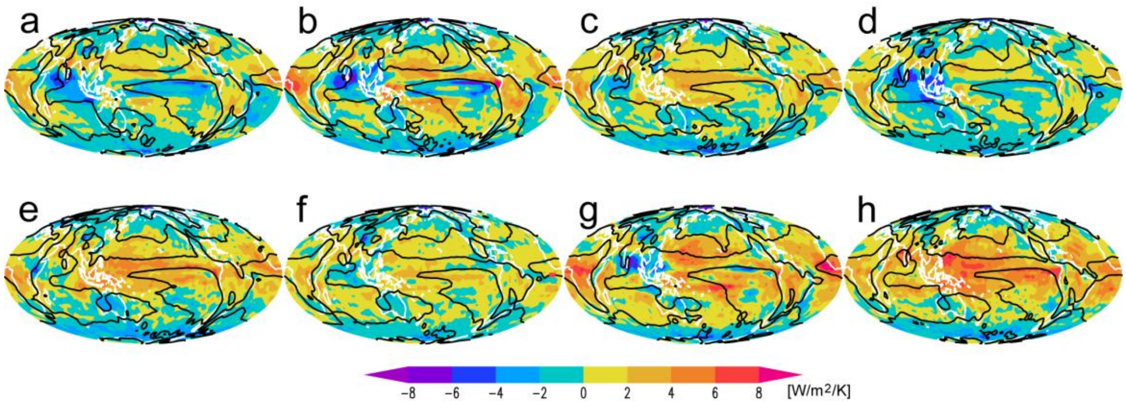

Figure 4 Spatial patterns of ΔSW_{cld} in MIROC5 MPE-A: (a) STD, (b) CLD, (c) CUM, (d) VDF, (e) CLD+CUM, (f) CUM+VDF, (g) CLD+VDF, and (h) CLD+CUM+VDF. The unit is W m^{-2} K^{-1}, and the zero contour of annual-mean ω in the control climate is imposed.

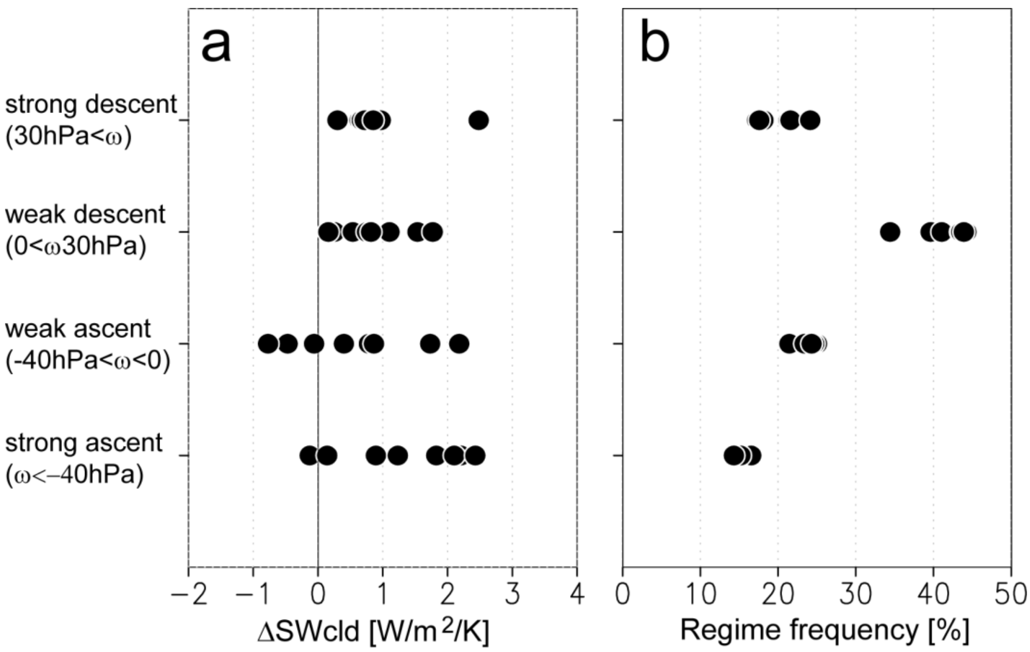

Figure 5 (a) Composite of ΔSW_{cld} over the tropics (30º S-30º N) with respect to four circulation regimes defined by ω. (b) As in (a) but for the regime frequency. Each model in MPE-A is indicated by a dot.

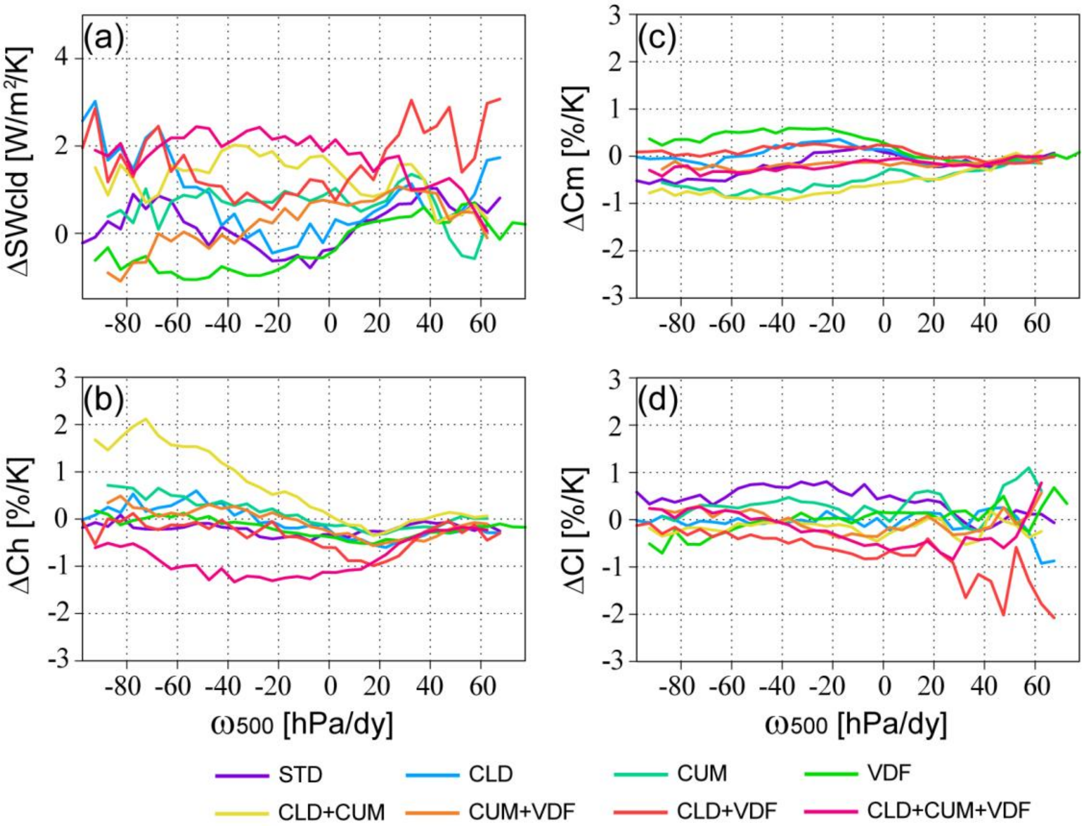

Figure 6 Regime composites of (a) ΔSW_{cld}, (b) ΔC_h, (c) ΔC_m, and (d) ΔC_l over the tropics (30º S-30º N) with respect to ω.

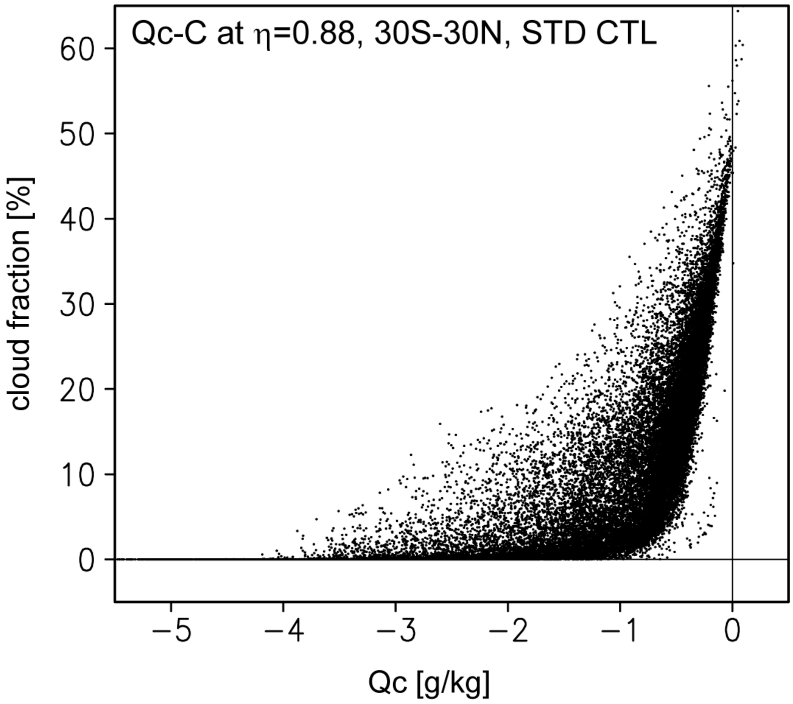

Figure 7 Scatter diagram of C against Q_c at η=0.88 over the tropics in the STD control run.

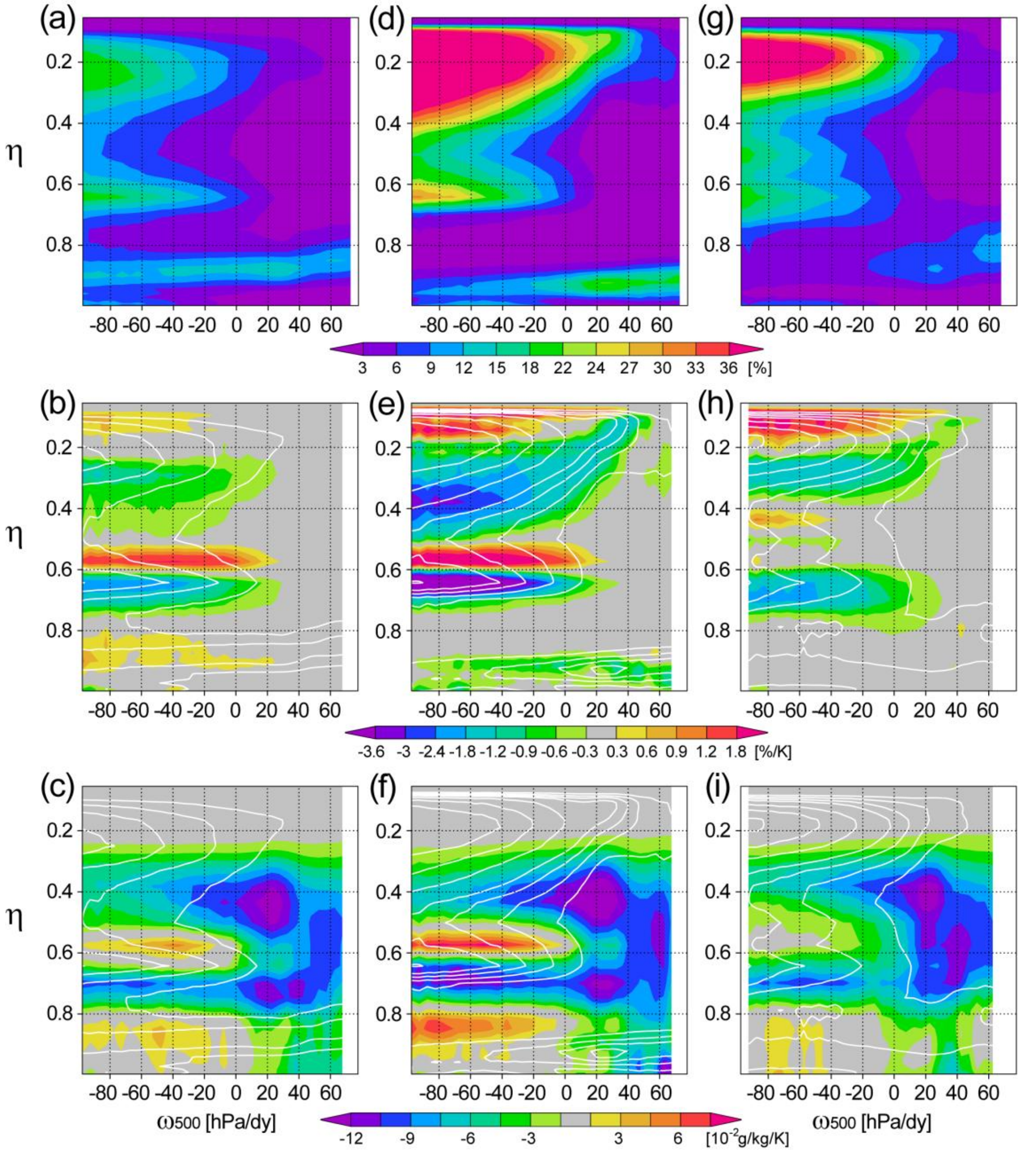

Figure 8 Regime composite of (a) C, (b) ΔC, and (c) ΔQ_c with respect to ω in STD. Values of C and ω are taken from the control run. Contours in (b)-(c) are the same as shading in (a). (d)-(f) As in (a)-(c) but for CLD+VDF. (g)-(i) As in (a)-(c) but for CLD+CUM.

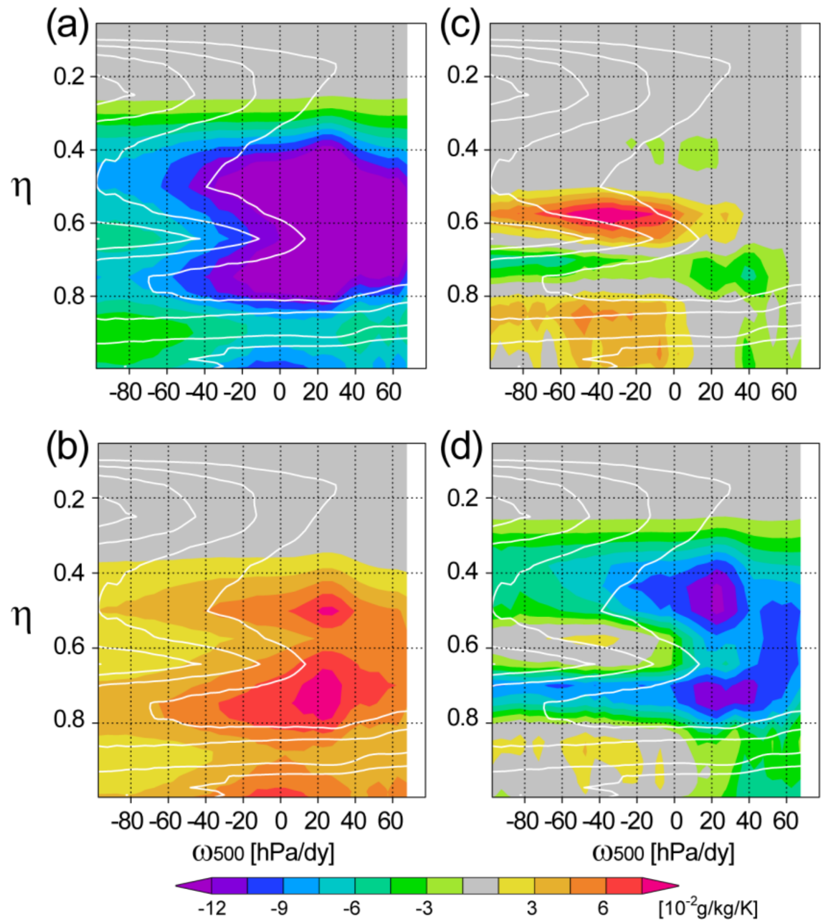

Figure 9 As in Fig. 8 but for dominant terms to ΔQ_c in STD: (a) temperature effect, (b) CC effect, (c) RH effect, and (d) sum of the three effects. Contours are the C composite in the control run (same as in Fig. 8b).

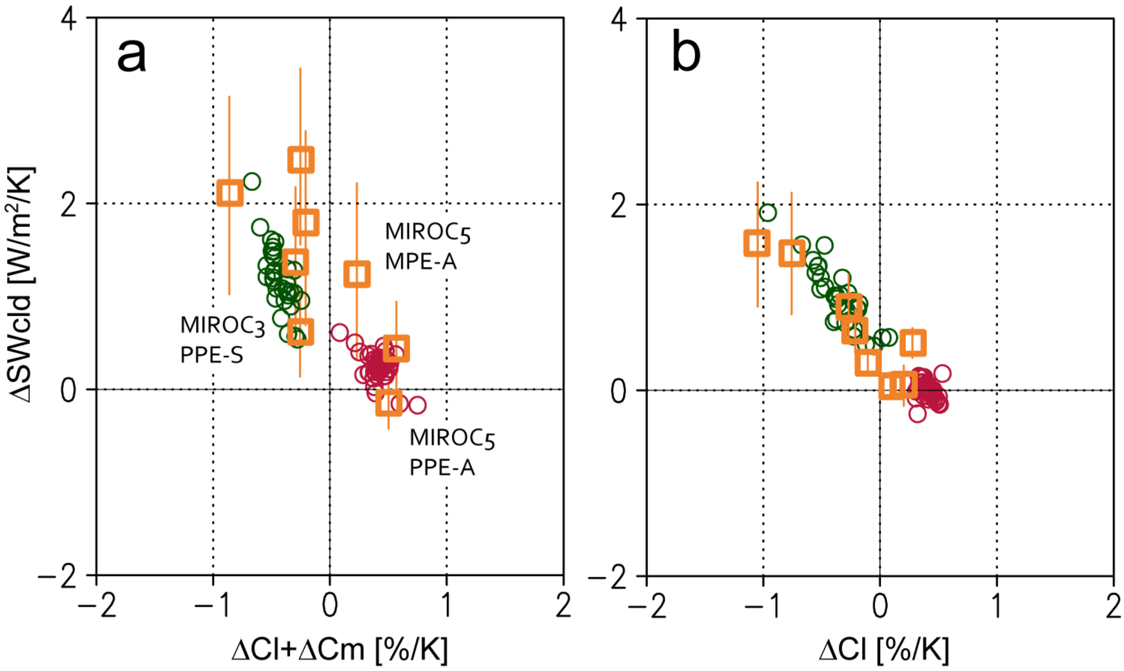

Figure 10 (a) Scatter diagram of ΔSW_{cld} against ΔC_l+ΔC_m over the convective regime ($\omega < 0$): MIROC3 PPE-S (green circles), MIROC5 PPE-A (red circles), and MIROC5 MPE-A (squares). The error bars for MPE indicate the range of the interannual variability. (b) As in (a) but for ΔSW_{cld} against ΔC_l over the subsidence regime ($\omega > 0$).

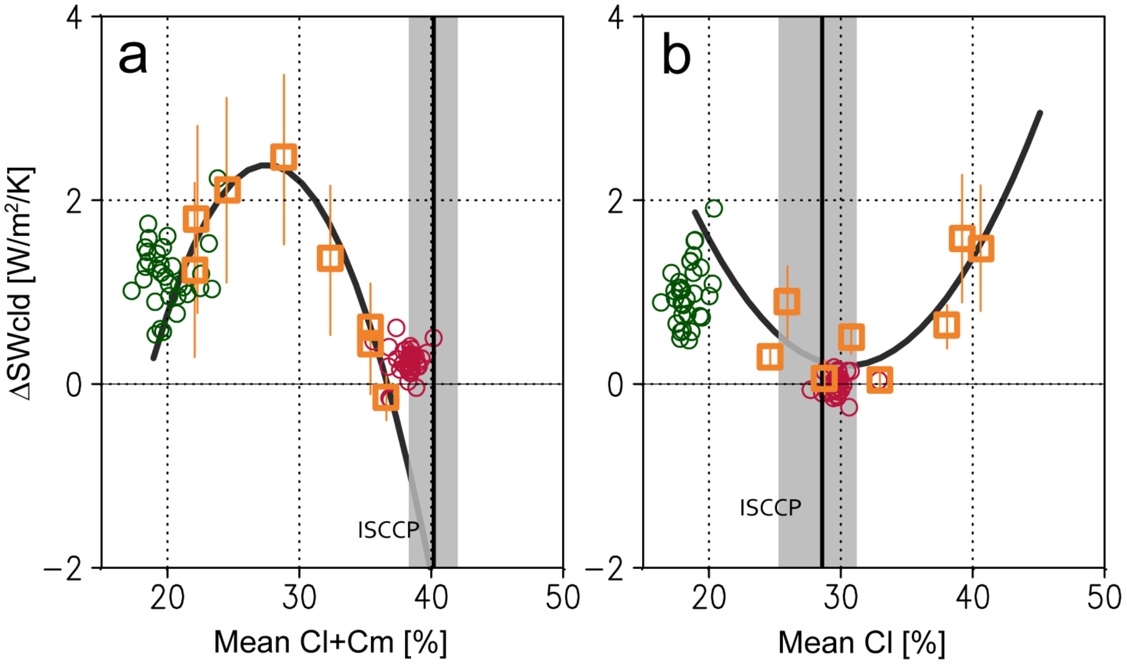

Figure 11 As in Fig. 10 but for ΔSW_{cld} against (a) $\bar{C}_l + \bar{C}_m$ for $\omega < 0$ and (b) $\bar{C}_l$ for $\omega > 0$. The thick vertical line with grey shading denotes the mean and the range of the interannual variability derived from ISCCP. Thick curves are the least-square fitted polynomials for the MIROC5 MPE-A.